Title

The rise, collapse, and compaction of Mt. Mantap from the 3 September 2017 North Korean nuclear test

Journal

Science, 361(6398)

ISSN

0036-8075

Authors

Wang, Teng
Shi, Qibin
Nikkhoo, Mehdi
et al.

Publication Date

2018-07-13

DOI

10.1126/science.aar7230

Peer reviewed

The rise, collapse, and compaction of Mt. Mantap from the 3 September 2017 North Korean nuclear test

Teng Wang[1]*, Qibin Shi[1,2], Mehdi Nikkhoo[3], Shengji Wei[1,2]*, Sylvain Barbot[1,2], Douglas Dreger[4]*, Roland Bürgmann[4], Mahdi Motagh[3,5], Qi-Fu Chen[6]

1 Earth Observatory of Singapore, Nanyang Technological University, Singapore. 2 Asian School of Environment, Nanyang Technological University, Singapore. 3 GFZ, German Research Centre for Geosciences, Potsdam, Germany. 4 Department of Earth and Planetary Science, University of California, Berkeley, CA, USA. 5 Institute for Photogrammetry and GeoInformation, Leibniz Universität Hannover, Hannover, Germany. 6 Key Laboratory of Earth and Planetary Physics, Institute of Geology and Geophysics, Chinese Academy of Sciences, Beijing, China. *Corresponding author. Email: wang.teng@ntu.edu.sg (T.W.); shjwei@ntu.edu.sg (S.W.); dreger@seismo.berkeley.edu (D.D.)

Abstract

Surveillance of clandestine nuclear tests relies on a global seismic network, but the potential of spaceborne monitoring has been underexploited. Here, we determined the complete surface displacement field of up to 3.5 m of divergent horizontal motion with 0.5 m of subsidence associated with North Korea's largest underground nuclear test using satellite radar imagery. Combining insight from geodetic and seismological remote sensing, we found that the aftermath of the initial explosive deformation involved subsidence associated with sub-surface collapse and aseismic compaction of the damaged rocks of the test site. The explosive yield from the nuclear detonation with seismic modeling for 450m depth was between 120-304 kt of TNT equivalent. Our results demonstrate the capability of spaceborne remote sensing to help characterize large underground nuclear tests.

Introduction

World peace benefits from the adherence to internationally negotiated nuclear-test-ban treaties that strive to promote the nonproliferation of nuclear weapons. In 2003, the Democratic People's Republic of Korea (North Korea) became the first country to withdraw from the 1968 Non-Proliferation treaty and started to conduct underground nuclear weapon tests with increasing intensity since 2006. On 3 September 2017, two seismic events separated by ~8.5 min were detected in the North Korea's Punggye-ri nuclear test site. Soon thereafter, North Korea's state media reported the successful firing of a two-stage thermonuclear bomb test. The US Geological Survey and China Earthquake Networks Center determined a body wave magnitude (m_b) of 6.3 for the first event (NKNT 6), much larger than the five nuclear tests since 2006 (NKNT 1-5). Shortly after, the scientific community started to determine the location, focal mechanism, and yield of the explosion using seismic waveforms and satellite optical imagery (*1*).

Preliminary analysis revealed a predominantly isotropic explosive source located beneath Mt. Mantap (*1*–*3*), which also hosted NKNT 2-5 (Fig. 1).

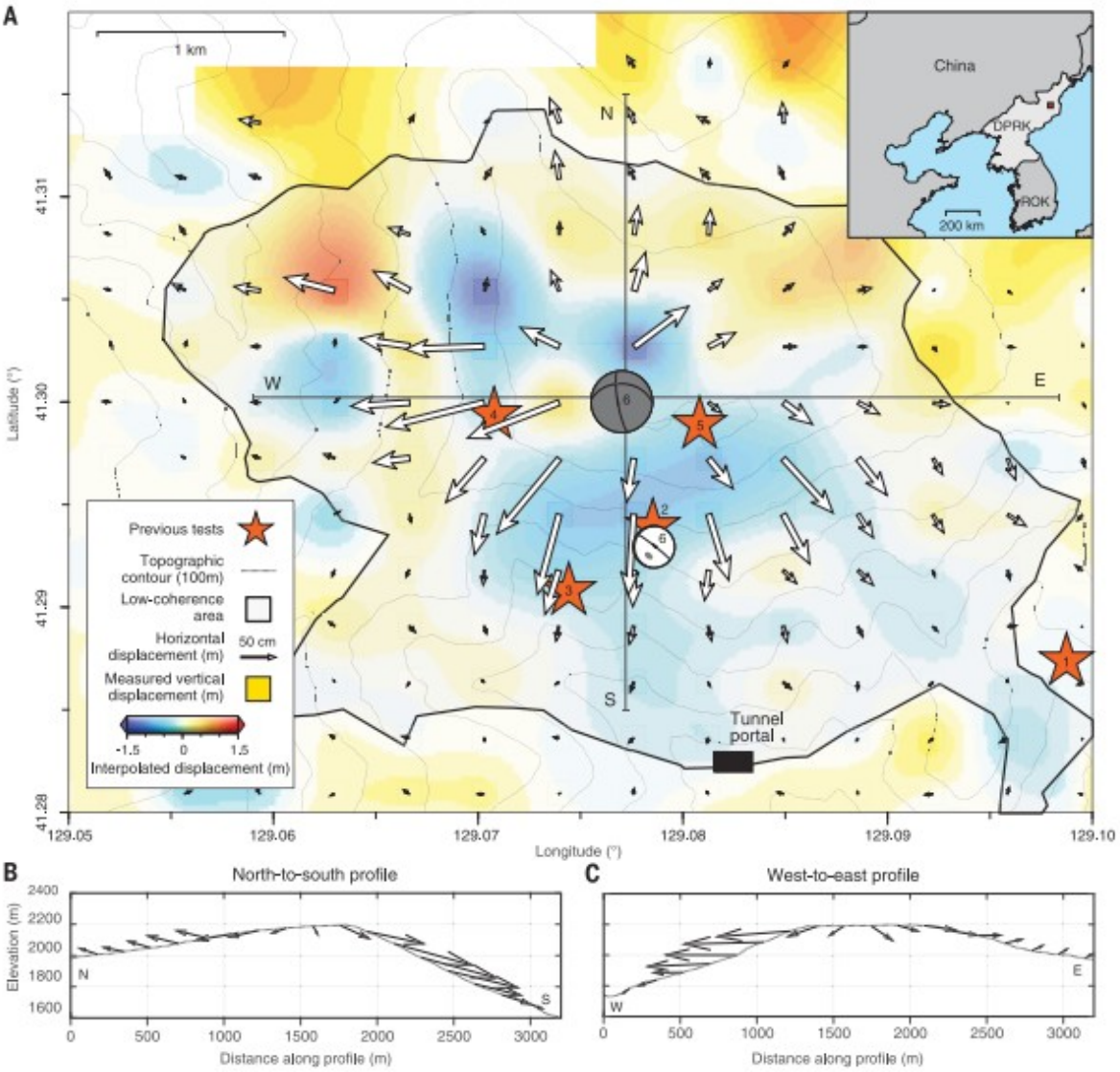

Fig. 1Three-dimensional (3D) displacement associated with the 3 September 2017 North Korean Nuclear Test (NKNT 6).

(A) 3D displacements derived from radar imagery with arrows indicating horizontal, color indicating vertical motions spanning the explosion and ~1 week of additional deformation. The uncertainties are shown in fig. S4 and provided in data S1 with the displacements. Black outline derived from ALOS-2 coherence loss indicates the substantial surface disturbance and large displacement gradients caused by the explosion over an area of ~9 km^2 (figs. S1 and S2). Thin gray lines are topographic contours at 100-m intervals. Red square in the upper right inset shows the location of Mt. Mantap. Red stars indicate the locations of NKNT 1-5 (*1*, *6*, *9*, *15*, *37*), among which NKNT 2-5 were all located within the NKNT-6 low-coherence region, NKNT 1 on 9 October 2006 was in a different location (*5*). Beach balls show locations and focal mechanisms of the M_w 5.24 and M_w 4.47 events on 3 September 2017.
(B and C) 2D (horizontal along the profile and vertical) displacements along two profiles across the top of Mt Mantap from north to south, and from west to east respectively. The elevations along the vertical axis in (B) and (C) are on scale.

The source properties of previous North Korean underground nuclear tests have been extensively studied using seismic waveforms (*4–12*), but surface displacements associated with these explosions are rarely reported. Remote sensing with Synthetic Aperture Radar (SAR) is a powerful technique for monitoring deformation of the Earth's surface (*13*, *14*) but its contribution to characterizing nuclear tests has been limited. The NKNT 4 conducted on 6 January 2016 has been studied using SAR interferometry, but the interpretation of interferometric phase is challenged due to the single imaging geometry (*15*). Tracking the amplitude features of the SAR images (so called pixel-offset tracking) is better suited when the interferometric phase is decorrelated (*16*). Moreover, pixel offsets can map displacement along the radar line-of-sight (LOS) and the satellite flying (azimuth) directions. In contrast to offset tracking of optical images, the SAR range offset is sensitive to the vertical displacement because of the slant-range imaging geometry, allowing for deriving three-dimensional (3D) displacements (*17–20*). Here we rely on detailed 3D displacements derived from sub-meter resolution SAR images together with seismic waveform data to reveal the complex processes that took place during and in the immediate aftermath of NKNT 6.

We measured the surface displacements caused by NKNT 6 by cross-correlating high-resolution spotlight radar images acquired by the German TerraSAR-X satellite, with an azimuth resolution of 1.1 m and a slant-range resolution as fine as 0.45 m (fig. S1 and table S1). The accuracy of the offset measurement is about 1/10 of the imaging resolution (*21*). We combined the azimuth and range offsets from two ascending and two descending tracks to calculate the total 3D surface displacements produced during and in the immediate aftermath of the explosion on a 300-by-300 m grid (Fig. 1 and figs. S3 to S5) (*22*). The horizontal motions of up to 3.5 m show a divergent pattern at the top of Mt. Mantap with a central zone of subsidence of ~0.5 m. We decomposed the 3D displacements into vertical and horizontal directions along two topographic profiles across the top of Mt. Mantap (Fig. 1). The along-profile displacements show that the horizontal displacement is generally larger where the topography is steeper (the west and south flanks). However, the direction of motion does not follow the slope of the terrain but is nearly horizontal. This indicates that while there is strong topographic control on the surface displacement field caused by the buried explosion, it does not resemble the slope-parallel motions expected from triggered landslides. While optical imagery suggests isolated 10-100 m scale landslide deposits (*23*), these appear to be debris flows localized in pre-existing channels that could not produce the large-scale horizontal motions we observed.

To resolve the horizontal location and depth of the detonation chamber, we set up numerical models that predict the surface displacements due to the expansion and subsequent collapse of an underground cavity embedded in a uniform elastic crust below realistic surface topography (*24*, *25*) (Fig. 2). We

constrained the 3D location of the source by minimizing the misfit between predicted and observed surface displacements (*26*, *27*). The explosion and immediate collapse of a 300 m radius spherical cavity that includes the detonation chamber and the surrounding damaged material reproduced the horizontal displacement well but was not sufficient to explain the small vertical motion around Mt Mantap. A third, mostly aseismic process involving the compaction of a larger volume is invoked to explain the low uplift (Fig. 2A and fig. S6). A similar compaction process has been inferred from the seismic analysis of other explosions (*28*) and was observed in the weeks to months following underground nuclear tests conducted in Nevada (*29*). As we do not have any constraints on the geometry of the compaction zone, we assumed a generalized ellipsoidal geometry for it and inferred its dimensions by using the geodetic observations. We estimated the explosive source to be located at 129.078°E/41.300°N±50 m, 1750 ± 100 m above mean sea level, i.e., 450 ± 100 m below the top of Mt. Mantap. Incorporating the large-scale compaction source into the model does not significantly influence our inferred epicenter of the explosion/collapse source (*22*).

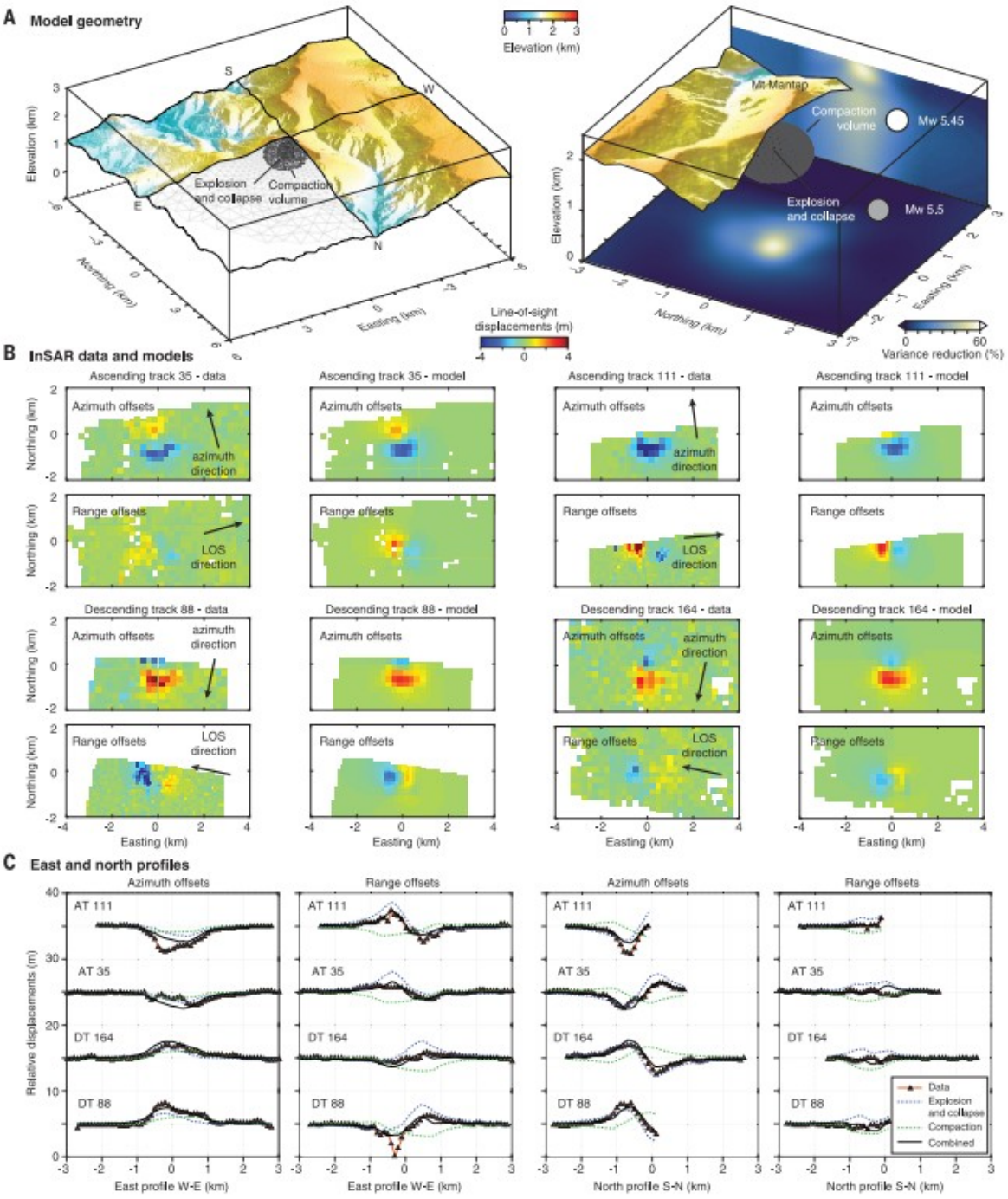

Fig. 2Model geometry and fit to the observed surface displacements.

(A) Perspective view of the model with topography and variance reductions as a function of centroid position (both cross-sections are centered on the best fit location). We represent the first event, combining the explosion and immediate collapse, using a sphere of 300 m radius with a centroid located at a depth about 450 m below Mt Mantap. We model the aseismic subsidence detected with geodetic data about a week after the seismic events 1 and 2 with an ellipsoid of dimension 800 × 800 × 470 m semi-axes, centered at 100 m deeper than the explosive source. The isotropic components of the moment tensors are represented as beach balls. (B) The observed and simulated surface displacements. (C) The west-east and south-north profiles of the surface displacements from the SAR observations and the best-fitting models. The dashed profiles represent the contributions of the

explosion/collapse (Event 1) and the subsequent aseismic compaction on the surface displacement. We ignore the deformation caused by Event 2.

Assuming that the hypocenter of the first event coincides with the center of the spherical cavity we refined the relative location for the second seismic event using local seismic waveform records from the NorthEast China Seismic Array to Investigate Deep Subduction (NECsaids) (*30*) and regional data from South Korean sites archived at the Incorporated Research Institutions for Seismology (IRIS) (Fig. 3A) (*22*). With the calibration from the first event and careful P-wave arrival picks of the second event (figs. S7 and S8), our grid search showed that the second event occurred 8 min 31.79 s after the first event and is located about 700 m to the south. Due to the azimuthal gap in the station coverage, the east-west location (±700m) is less well constrained compared with the north-south separation (±200m with 96% confidence) (Fig. 3C and fig. S9). The refined location of the second implosive event is beneath the area of large subsidence and southward horizontal motion under the south flank of Mt. Mantap, between the initial explosion and the south portal of the tunnel system (Fig. 1).

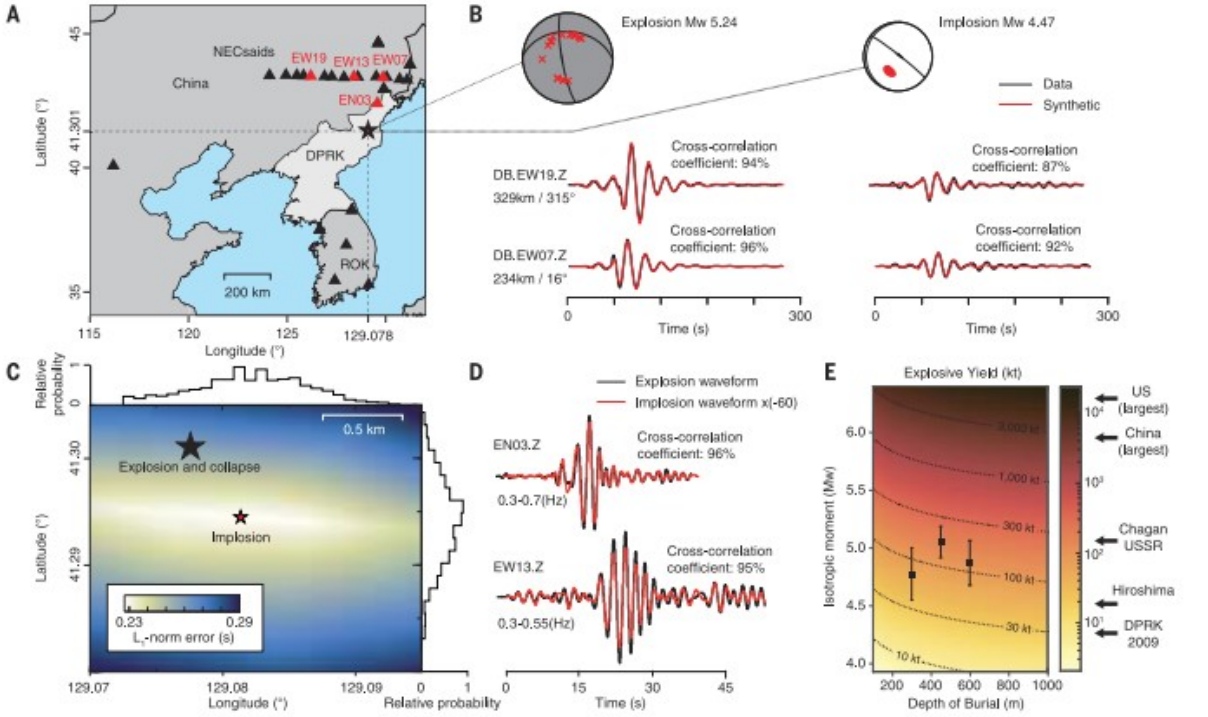

Fig. 3Analysis of seismic waves.

(A) Station map of broadband seismometers with four stations in (B) and (D) highlighted in red. The black and red stars are the epicenter location of the first and second event, respectively. (B) Moment tensor solutions for the first explosive (left) and the second implosive (right) event, with vertical component of two representative stations shown at the bottom. Both data and synthetics are filtered between 0.02 and 0.045 Hz. Station names are shown at the beginning of waveform pairs and distance (in km) and azimuth (in degree) are indicated below. (C) Grid search result (under L1 norm) for relocating the second event relative to the first event (black star). Marginal distribution for the epicentral position are plotted along the northing and easting axes. (D) Vertical component waveform comparison between the first (black) and the second (red) event at two representative stations, with the second event waveforms multiplied by -60. (E) Explosive yield with historical nuclear tests. The

black dots and error bars show yields estimated based on the mean and standard deviation of tabulated moment within 95% of the best fitting solutions with depths of 300, 450 and 600 m respectively.

We applied the generalized Cut-And-Paste (gCAP) method (*31*) to the regional and local waveform data to invert for the full moment tensor solutions of the two seismic events, including isotropic (i.e., explosive or implosive volume source), compensated-linear-vector-dipole (CLVD) (i.e., ring faulting along a certain axis, like a collapse), and double-couple (i.e., shear dislocation on planar fault) components (*22*). Our preferred solution of the first event indicates a moment of 9.5×10^{16} N m ($M_w = 5.24$) and a 50-90% positive isotropic component, and relatively small CLVD or double couple contributions (figs. S10 to S13). The second seismic event ($M_w = 4.5$) has a large negative isotropic component (~50-70% of the total moment) (figs. S14 and S15). While we obtained a high waveform cross-correlation coefficient between the data and synthetics for most of the waveform components of the first event (e.g., Fig. 3B), the noise level for the second event is larger, resulting in a much smaller variance reduction of the observations (fig. S16). To overcome this limitation of the data, we drew insight on the moment tensor of the second event by directly comparing the waveforms with those of the first event. We multiplied the amplitude of the vertical-component waveforms of the second event by a factor of -60 and compared them with the waveforms of the first event at higher frequencies (~0.2-0.9 Hz). The result (Fig. 3D and fig. S16) shows very high waveform cross-correlation coefficients, even for some coda waves, supporting the close locations but opposite isotropic polarities of the two events (*2*).

Combining the depth constraints from geodesy and energy constraints from seismology, we can refine the explosive yield of the nuclear explosion (*32*–*34*). We assumed the seismic velocity model MDJ2 (*4*) for the elastic earth structure. We based the overburden pressure on the best-fitting centroid source depth of 450 ± 100 m from the geodetic modeling. The medium in which the device was detonated was likely the granodiorite that lies beneath the stratified volcanic rocks that make up the high elevations of Mt. Mantap (*8*). We assumed a gas porosity of 1% for granitic rocks (*35*). Considering an isotropic seismic moment of magnitude $M_w = 5.05$ (the mean value of solutions fitting within 95% of the maximum fit for a source depth of 450m) and the possible range of source depths of 350-550 m, the yield estimates range between 171-209 kt of TNT equivalent, with 191 kt corresponding to the best-fitting source parameters from geodetic and seismic data (Fig. 3E). Doubling the gas porosity results in an 8% increase in the magnitude of estimated yield.

The source characteristics we derived from surface displacement and seismic waveforms are in remarkable agreement. The divergent horizontal motions and the moment tensor of the first event consistently suggest a predominant isotropic explosive source buried at shallow depth. The moment of the geodesy-derived models, assuming an empirical rigidity of 5.7 GPa

(*36*), is M_w = 5.5, larger than the one inferred seismically (M_w = 5.24), because it includes slow deformation that did not generate seismic waves - with a total volume change of 0.01 km^3. The seismic analysis of the second event reveals an implosive seismic source that occurred south of the first event with a dominant negative isotropic component, suggesting an inverse process of the main explosion. This may reflect the combination of negative isotropic compaction of the over-pressured cavity and/or vertical collapse of the explosion chimney and nearby tunnel segments due to gravity, contributing to the subsidence on the south flank of Mt. Mantap (Fig. 4). The larger-scale compaction source in the geodetic model is independent of the first and second seismic events, and the post-explosion compaction of surrounding rocks may continue aseismically for an extended period, as seen in the Nevada underground nuclear test site with initial subsidence rates of ~1-7 cm/yr (*29*).

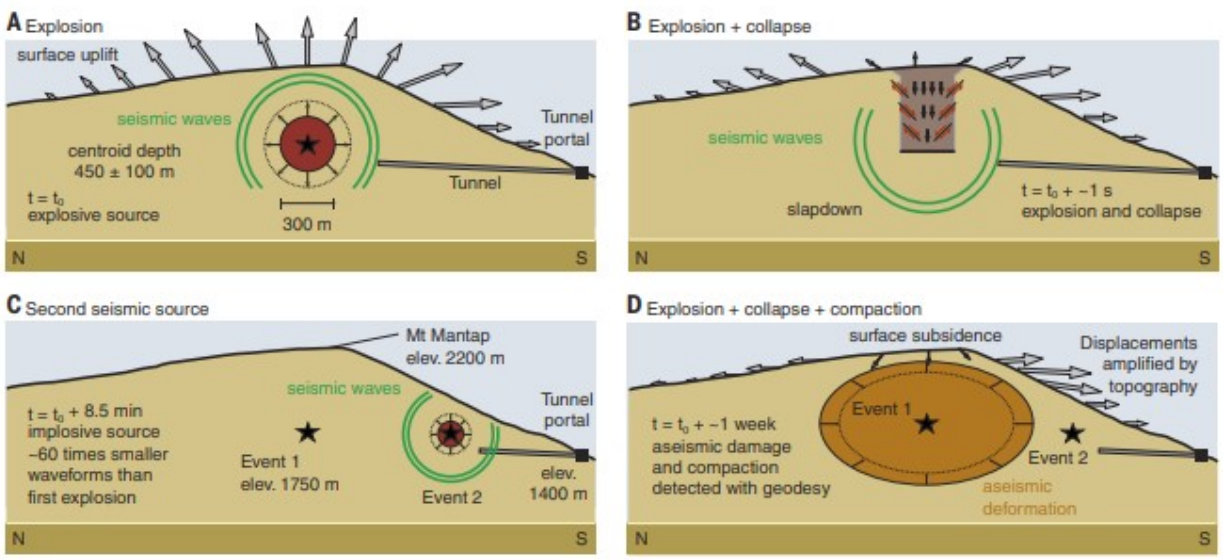

Fig. 4Summary deformation scenario for the 3 September 2017 North Korea's Nuclear test.

The unfolding of events includes the succession of (A) explosive, (B) collapse, and (D) compaction processes, with different associated surface displacements. The implosive source (C) may be shallow and only contribute localized surface displacements. The radar imagery reveals the deformation (arrows in (D)] resulting from the three processes.

Our 3D surface displacement measurements and elastic modeling incorporating realistic topography allow for locating the main explosive event within ±50 m assuming a uniform elastic medium, but a non-uniform structure and small-scale surficial processes (e.g., landslides) may bias our results. As the largest deformation occurred above the explosive source due to the chimneying and spalling effect (*28*), the centroid of the modeled geodetic source may locate above the actual detonation point. Following the explosion, water was observed to be flowing from the tunnel portal (*23*). Assuming a slope of 2-4 degrees to provide drainage, the depth implied from the elevation of the tunnel entrance is about 600-700 m below the surface,

consistent with a detonation point about 150 m deeper than the centroid of geodetic model.

Combining the available space-borne geodetic and seismic records provided new insights into the mechanics of deformation surrounding North Korea's sixth underground nuclear test, revealing the explosion, collapse, and subsequent compaction sequence (Fig. 4). The modeling of the geodetic observations reduces the epicentral and depth uncertainties that otherwise hinder the analysis of seismic waveforms. The derived horizontal location of the first event is important to relatively relocate the second event, which likely indicates the collapse of the tunnel system of the test site. The inclusion of geodetic data also helps resolving the aseismic deformation processes that may follow nuclear tests. Finally, our findings demonstrate the capability of monitoring shallow underground nuclear tests using remote-sensing observations and seismic sensors.

References and Notes

1. Incorporated Research Institutions for Seismology, "Special event: 2017 North Korean nuclear test"; http://ds.iris.edu/ds/nodes/dmc/specialevents/2017/09/03/2017-north-koreannuclear-test/. 2. J. Liu et al., Geophys. Res. Lett. 10.1002/2018GL077095 (2018). 3. D. Tian, J. Yao, L. Wen, Geophys. Res. Lett. 10.1029/ 2018GL077649 (2018). 4. S. Ford, D. Dreger, W. Walter, Geophys. Res. Lett. 36, L21304 (2009). 5. N. Selby, Bull. Seismol. Soc. Am. 100, 1779–1784 (2010). 6. L. Wen, H. Long, Seismol. Res. Lett. 81, 26–29 (2010). 7. K.-Y. Chun, Y. Wu, G. Henderson, Bull. Seismol. Soc. Am. 101, 1315–1329 (2011). 8. E. Rougier, H. J. Patton, E. E. Knight, C. R. Bradley, Geophys. Res. Lett. 38, L16316 (2011). 9. L. F. Zhao, X. B. Xie, W. M. Wang, Z. X. Yao, Bull. Seismol. Soc. Am. 102, 467–478 (2012). 10. M. Zhang, L. Wen, Geophys. Res. Lett. 40, 2941–2946 (2013). 11. L.-F. Zhao, X.-B. Xie, W.-M. Wang, Z.-X. Yao, Seismol. Res. Lett. 85, 130–134 (2014). 12. S. Cesca, S. Heimann, M. Kriegerowski, J. Saul, T. Dahm, Seismol. Res. Lett. 88, 300–310 (2017). 13. J. Hu et al., Earth Sci. Rev. 133, 1–17 (2014). 14. J. R. Elliott, R. J. Walters, T. J. Wright, Nat. Commun. 7, 13844 (2016). 15. M. Wei, Geophys. J. Int. 209, 762–769 (2017). 16. R. Michel, J.-P. Avouac, J. Taboury, Geophys. Res. Lett. 26, 875–878 (1999). 17. E. Pathier et al., Geophys. Res. Lett. 33, L20310 (2006). 18. T. Wang, S. Jonsson, IEEE J. Sel. Top. Appl. Earth Obs. Remote Sens. 8, 3271–3278 (2015). 19. J. Ruch, T. Wang, W. Xu, M. Hensch, S. Jónsson, Nat. Commun. 7, 12352 (2016). 20. L. N. Schaefer et al., Geophys. Res. Lett. 44, 135–142 (2017). 21. R. Bamler, M. Eineder, IEEE Geosci. Remote Sens. Lett. 2, 151–155 (2005). 22. See supplementary materials. 23. F. V. Pabian, J. S. Bermudez Jr., J. Liu, North Korea's Punggye-ri Nuclear Test Site: Satellite Imagery Shows Post-Test Effects and New Activity in Alternate Tunnel Portal Areas (2017); www.38north.org/2017/09/punggye091217/. 24. M. Nikkhoo, T. R. Walter, Geophys. J. Int. 201, 1117–1139 (2015). 25. M. Nikkhoo, T. R. Walter, P. R. Lundgren, P. Prats-Iraola, Geophys. J. Int. 208, 877–894 (2017). 26. J. H. Holland, Adaptation in Natural and Artificial Systems (Univ. of Michigan

Press, 1975). 27. R. L. Haupt, S. E. Haupt, Practical Genetic Algorithms (Wiley, ed. 2, 2004). 28. H. J. Patton, S. R. Taylor, J. Geophys. Res. Solid Earth 116, B03310 (2011). 29. P. Vincent et al., Geophys. Res. Lett. 30, 1–5 (2003). 30. X. Wang, Q.-F. Chen, J. Li, S. Wei, Seismol. Res. Lett. 87, 901–911 (2016). 31. L. Zhu, Y. Ben-Zion, Geophys. J. Int. 194, 839–843 (2013). 32. E. Teller, W. K. Talley, G. H. Higgins, G. W. Johnson, The Constructive Uses of Nuclear Explosives (McGraw-Hill, 1968). 33. M. D. Denny, L. R. Johnson, in Explosion Source Phenomenology, S. R. Taylor, H. J. Patton, P. G. Richards, Eds. (American Geophysical Union, 1991), pp. 1–24. 34. S. R. Ford, W. R. Walter, Bull. Seismol. Soc. Am. 103, 2937–2945 (2013). 35. D. L. Springer, Bull. Seismol. Soc. Am. 56, 861–876 (1966). 36. D. L. Springer, G. A. Pawloski, J. L. Ricca, R. F. Rohrer, D. K. Smith, Bull. Seismol. Soc. Am. 92, 1806–1840 (2002). 37. S. J. Gibbons, F. Pabian, S. P. Näsholm, T. Kværna, S. Mykkeltveit, Geophys. J. Int. 208, 101–117 (2016)

Acknowledgments: We thank three anonymous reviewers for their comments. Funding: T.W., Q.S., S.W., S.B. at Earth Observatory of Singapore (EOS) are supported by the Singapore Ministry of Education under the Research Centres of Excellence initiative, the National Research Foundation (NRF) of Singapore under the NRF Fellowship scheme (National Research Fellow Award NRF-NRFF2013-04), EOS startup fund M4430240.B50, and Ministry of Education Singapore Academic Research Fund Tier 1 RG181/16. M.N. is supported by VOLCAPSE, a research project funded by the European Research Council under the European Union’s H2020 Programme/ERC consolidator grant No. [ERC-CoG 646858]. D. D. was is supported by the Air Force Research Laboratory contract no. FA9453-16-C-0024. Q.-F.C. is supported by the National Science Foundation of China grant No. 41474041. This work comprises Earth Observatory of Singapore contribution no. 185. Author contributions: T.W. analyzed SAR images provided by M.M, Q.S. and S.W. conducted the seismic analysis using the data collected by Q-F. C., M.N. and S.B conducted the geodetic modeling, D.D. estimated the yield, T.W., M.N., S.B., R.B., and M.M contributed to the interpretation of SAR offsets and geodetic models; Q.S., S.W., D.D. and Q-F. C. contributed to the interpretation of seismic waves and moment tensors. T.W. drafted the manuscript with inputs from all co-authors. Competing interests: All authors declare no conflicts of interest. Data and materials availability:The TerraSAR-X images are copyright of German Aerospace Agency (DLR) and provided under proposal motagh_GGEO1217. The ALOS-2 images are provided by JAXA under the ALOS-2 RA4 Research Project 1413 and 1161. SAR offsets, 3D displacement data points and regional seismic waveform data are provided in the supplementary material. Tele-seismic data are archived at the Incorporated Research Institutions for Seismology (IRIS).